JOURNAL OF
APPLIED
CRYSTALLOGRAPHY

ISSN 1600-5767

An insight into the synthesis, crystal structure, geometrical modelling of crystal morphology, Hirshfeld surface analysis and characterization of *N*-(4-methylbenzyl)benzamide single crystals

Sahil Goel,[a] Harsh Yadav,[a] Nidhi Sinha,[b] Budhendra Singh,[c] Igor Bdikin,[c] Devarapalli Chenna Rao,[d] Kovuru Gopalaiah[d]* and Binay Kumar[a]*

[a]Crystal Lab, Department of Physics and Astrophysics, University of Delhi, Delhi 110007, India, [b]Department of Electronics, SGTB Khalsa College, University of Delhi, Delhi 110007, India, [c]TEMA-NRD, Mechanical Engineering Department, Aveiro Institute of Nanotechnology (AIN), University of Aveiro, Aveiro 3810-193, Portugal, and [d]Organic Synthesis and Catalysis Laboratory, Department of Chemistry, University of Delhi, Delhi 110007, India. *Correspondence e-mail: gopal@chemistry.du.ac.in, b3kumar69@yahoo.co.in

Received 16 May 2017
Accepted 24 August 2017

Edited by F. Meilleur, Oak Ridge National Laboratory, USA, and North Carolina State University, USA

Keywords: *N*-(4-methylbenzyl)benzamide; crystal structure; crystal morphology; centre of mass propagation vector; Hirshfeld surface analysis; photoluminescence; piezoelectricity.

CCDC reference: 1524601

Supporting information: this article has supporting information at journals.iucr.org/j

A versatile approach for the synthesis of *N*-(4-methylbenzyl)benzamide, $C_{15}H_{15}NO$, using CuI as catalyst has been reported. Single crystals of the synthesized compound were grown using the slow evaporation solution technique. The crystal structure of the *N*-(4-methylbenzyl)benzamide crystals has been determined by single-crystal X-ray diffraction. The compound crystallizes in an orthorhombic lattice, noncentrosymmetric space group $Pna2_1$. The crystal structure is stabilized by intermolecular $\mathrm{N-H\cdots O}$ hydrogen bonds and weak $\mathrm{C-H}\cdots\pi$ interactions to form layers parallel to the *a* axis. A user-friendly approach based on centre of mass propagation vector theory was used to predict the crystal morphology. The framework developed here utilizes the concept of intermolecular bond strength to discern the crystal morphology. Fourier transform IR, NMR and high-resolution mass spectrometry analytical techniques were used for the identification of functional groups and confirmation of the structure of the title compound. All of the intermolecular interactions present in the crystal structure, including the $\mathrm{C-H}\cdots\pi$, $\mathrm{C-H\cdots O}$ and $\mathrm{N-H\cdots O}$ interactions, were investigated and confirmed by molecular Hirshfeld surface analysis. From linear optical spectroscopy, the transmittance, optical band gap and UV cutoff wavelength were determined. The photoluminescence emission spectrum was recorded for a grown crystal. Dielectric measurements were performed at room temperature for various frequencies. The mechanical strength of the (001) plane of the title compound was measured using the Vickers micro-hardness technique. A piezo-coefficient of 15 $\mathrm{pC\,N^{-1}}$ was found along the (001) plane of the title crystals. The thermal stability and melting point were also investigated. In addition, density functional theory simulations were used to calculate the optimized molecular geometry and the UV–vis spectrum, and to determine the highest occupied molecular orbital/lowest unoccupied molecular orbital energy gap. The results show that *N*-(4-methylbenzyl)benzamide is a potential candidate for multifunctional optical and piezoelectric crystals.

1. Introduction

In the field of molecular electronics, the enormous demand for low power consumption, cheap and flexible electronics, and the design of energy-efficient harvesting devices is attracting the attention of researchers to synthesize and develop energy-efficient organic molecular crystals (Gundlach, 2007; Kippelen & Brédas, 2009; Klauk *et al.*, 2007). The ability to exhibit high symmetry, which allows monomeric organic molecules to form large supramolecular chains of specific symmetry, qualifies

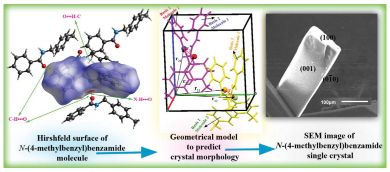

compounds based on such molecules as better alternatives to organic polymer-based materials, helping to reduce the cost of real world consumer electronics (Brooks, 2010). In organic crystals, the intermolecular interactions present in the molecular packing greatly influence their optoelectronic and piezoelectric properties. In natural as well as synthetic chemicals, amide functionality constitutes an important scaffold (Saha *et al.*, 2014). The amide group acts as a basic skeletal linkage in the peptide chain of proteins, pharmaceuticals, polymers, agrochemicals and bio-potent organic molecules (Han & Kim, 2014; Nageswara Rao *et al.*, 2014). Because of the relatively inert and poor electrophilic nature of the amide group, the nucleophiles need either harsh reaction conditions or complex reaction mechanisms, which lead to the transamidation of the amides with amines under high-temperature conditions (Durgaiah *et al.*, 2016). Although the Ritter reaction is a well established and extensively used method for the preparation of a wide range of amides, lactams and other heterocycles, the classical experimental procedure is cumbersome. Moreover, amides could be synthesized by coupling of carboxylic acids, alcohols and aldehydes with amines, hydroamination of alkynes, and hydration of nitriles using stoichiometric quantities of reagents and harsh reaction conditions (Nageswara Rao *et al.*, 2014). Therefore, the catalytic approach is in high demand to improve the method for the synthesis of carboxamide derivatives (Nammalwar *et al.*, 2015).

The molecular structure of *N*-(4-methylbenzyl)benzamide, $C_{15}H_{15}NO$, consists of *p*-methylbenzylamine and benzoyl scaffolds. Benzamide compounds show various pharmacological activities like antiarrythmic, antipsychotic and antiemetic properties (Bülbül *et al.*, 2015). In the case of *N*-substituted derivatives of benzamide, anticonvulsant activity is present (Revathi *et al.*, 2015). However, some other benzamide compounds act as potent Kv1.3 inhibitors and Kv1.3 ion channel blockers (Haffner, Thomson, Guo, Petrov *et al.*, 2010; Haffner, Thomson, Guo, Schaller *et al.*, 2010). Recently, Elbagerma *et al.* (2010) investigated the formation of co-crystals from equimolar quantities of salicylic acid and benzamide for the enhancement of the physiochemical properties of the active pharmaceutical ingredient without changing the pharmaceutical activity.

However, there are only a few reports available on the synthesis of *N*-(4-methylbenzyl)benzamide (Karabulut & Kacan, 2002; Kerdphon *et al.*, 2015; Shen *et al.*, 2008). In many of these reports, harsh reaction conditions were employed for the optimization of the reaction, using heavy metals as catalysts. The literature also reports several similar crystal structures, such as *N*-(4-methylphenyl)benzamide (Gowda, Tokarčík, Kožíšek & Sowmya, 2008), 2,6-dichloro-*N*-(4-methylphenyl)benzamide (Wei *et al.*, 2012), *N*-phenylbenzamide (Bowes *et al.*, 2003), 2-methyl-*N*-(4-methylphenyl)benzamide (Gowda, Tokarčík, Kožíšek, Sowmya & Fuess, 2008), 2-methyl-*N*-*p*-tolylbenzamide (Saeed *et al.*, 2010) *etc.* Luo & Huangn (2004) have reported the solid phase synthesis and crystal structure of *N*-(4-methylbenzyl)benzamide. However, to our knowledge, no further investigations have been carried out to determine the growth, dielectric, piezoelectric, optical and mechanical properties of the *N*-(4-methylbenzyl)benzamide crystal.

In the present work, we synthesized *N*-(4-methylbenzyl)benzamide ($C_{15}H_{15}NO$; MBB) from *p*-methyl benzylamine and benzaldehyde under mild conditions using CuI as a catalyst and *tert*-butylhydroperoxide (TBHP) as an oxidant. The synthesized compound was crystallized by the slow evaporation technique using hexane/ethyl acetate (EtOAc) (5:1) solution and the obtained crystals were employed for further experimental measurements. Herein, systematic studies have been conducted to determine the growth and crystal structure and to perform conformational and spectroscopic analysis of the MBB single crystals. The crystals were characterized using Fourier transform infrared spectroscopy (FTIR), ^{1}H and ^{13}C nuclear magnetic resonance, high-resolution mass spectrometry (HRMS), UV–vis–NIR spectroscopy, photoluminescence spectroscopy, and dielectric, piezoelectric, mechanical and thermal studies. In addition, a visual identification of all the intermolecular interactions present in the crystal packing was achieved using three-dimensional Hirshfeld surfaces and two-dimensional fingerprint plot analysis. The theoretically optimized molecular geometry, UV–vis absorbance spectrum and highest occupied molecular orbital/lowest unoccupied molecular orbital (HOMO–LUMO) energy levels were simulated using density functional theory (DFT) and were compared with the experimentally observed results.

In one of our previous reports, we described a simple algorithm to predict the crystal morphology and the growth rate of the crystal plane, derived from the propagation vector of the centre of mass of the molecular basis present in the crystal lattice (Yadav, Sinha & Kumar, 2016). The proposed theory was successfully employed to predict the morphologies of L-prolinium tartrate, benzophenone and benzil crystals, which were found to be in good agreement with the experimentally observed morphologies (Yadav, Sinha & Kumar, 2016). In the present report, the experimentally observed morphology of the MBB crystals was studied on the basis of our centre of mass propagation vector theory, denoted HNB vector (Harsh–Nidhi–Binay). The morphology derived from this theory was compared with the morphology predicted by existing models [Bravais–Friedel–Donnay–Harker (BFDH) law (Docherty *et al.*, 1991) and Hartman–Perdok (HP) theory (Hartman & Perdok, 1955)].

2. Experimental

2.1. Synthesis and crystal growth

To a suspension of 4-methylbenzylamine (1.0 mmol) dissolved in dry dimethyl sulfoxide in a round-bottomed flask, benzaldehyde (1.0 mmol) and CuI (5 mol%) were added at room temperature (RT) under nitrogen atmosphere. The reaction mixture was stirred at 353 K for 6 h. Then, the flask was cooled to room temperature, and TBHP (1.0 mmol) was added dropwise. The resulting mixture was heated at 353 K for

10 h. The reaction flask was cooled to room temperature and the crude material was extracted with ethyl acetate (15 ml) and water (25 ml). The organic layer was separated and dried over anhydrous sodium sulfate, filtered off, and concentrated under reduced pressure. The crude compound was purified by silica gel column chromatography using hexane/EtOAc as mobile phase, resulting in *N*-(4-methylbenzyl)benzamide in 82% yield as a colourless solid. The scheme below is a graphical representation of the reaction described above. The product isolated by column chromatography was dissolved in a hexane/EtOAc (5:1) solvent system. The solution was kept for slow evaporation. After a time span of 2 d, fine needle-shaped crystals suitable for our studies were harvested. Photographs, a scanning electron microscope image and the indexed graphical morphology are shown in Fig. 1.

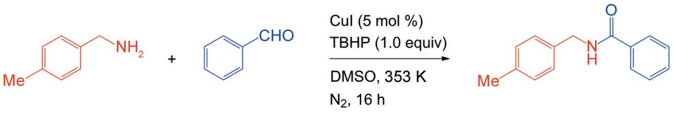

2.2. Characterization techniques

A single-crystal X-ray diffraction (SCXRD) analysis of the MBB crystals was performed in the ω scan mode on an Oxford Xcalibur diffractometer (Mo *Kα* X-ray source, $\lambda = 0.71073$ Å). A single crystal of dimension 0.5 × 0.5 × 0.5 mm was selected for SCXRD measurement. Hirshfeld surfaces for the title crystal mapped over normalized contact distance, shape index, curvedness and electrostatic potential were generated using *CrystalExplorer 3.1* (Wolff *et al.*, 2012). The electrostatic potentials were mapped over the Hirshfeld surface with the aid of the *TONTO* program using a STO-3G basis set (Hartree–Fock theory) (Spackman *et al.*, 2008). The empty space in the crystal lattice was analysed using void mapping (*CrystalExplorer 3.1*). The FTIR spectrum for the MBB crystals was recorded in the infrared range 4000–600 cm^{-1} employing a PerkinElmer RXI FTIR spectrophotometer in dichloromethane solution. The ^{1}H NMR spectrum was recorded on a JEOL 400 MHz spectrometer (JNM-EXCP 400) in CDCl$_3$; chemical shifts (δ p.p.m.) and coupling constants (Hz) are reported in the standard fashion with reference to internal standard tetramethylsilane ($\delta_{\rm H}$ = 0.00 p.p.m.). The ^{13}C NMR spectrum was recorded on a 100 MHz spectrometer (JNM-EXCP 400); chemical shifts (δ p.p.m.) are reported relative to CDCl$_3$ ($\delta_{\rm C}$ = 77.00 p.p.m., central line of triplet). The high-resolution mass spectrum was recorded on an electrospray quadrupole time-of-flight mass spectrometer [Agilent, G6530AA (LC-HRMS-Q-TOF)]. The UV–vis transmittance spectrum was measured using a SHIMADZU UV-2501PC in the wavelength range 200–1100 nm. The photoluminescence (PL) emission spectrum of the solid material was measured on a Horiba Jobin Yvon Fluorolog modular spectro-fluorometer using a continuous-wave xenon lamp source. An Agilent E4980A LCR meter was used to measure the dielectric properties at room temperature, with a frequency range of 20 Hz−2 MHz. The piezo-coefficient of the MMB crystals was measured using a piezometer (PM 300, Piezotest) at a tapping force and tapping frequency of 0.25 N and 110 Hz, respectively. A Vickers micro-hardness MVH-I (Omni Tech) tester was used to characterize the mechanical strength of the material under a fixed dwell time of 5 s. Thermogravimetric analysis on the MBB crystals was performed using a PerkinElmer Diamond thermogravimetric/differential thermal analysis (TG/DTA) analyser in a nitrogen atmosphere at a heating rate of 10 K min^{-1} in the temperature range from 308 to 723 K.

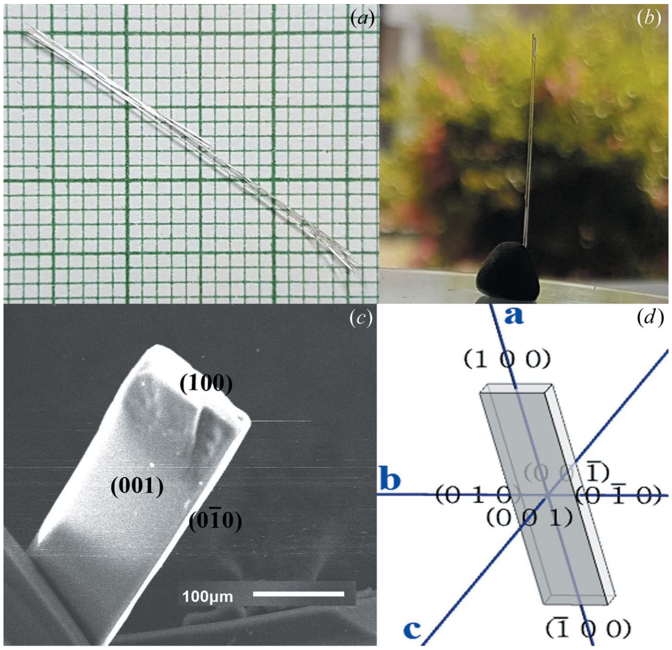

Figure 1
(*a*), (*b*) Photographs of as-grown MBB single crystals. (*c*) High-magnification scanning electron microscope image of an MBB crystal along with Miller indexing of various crystal faces. (*d*) Indexed graphical morphology of the MBB crystal.

2.3. Computational details

All DFT calculations were performed using the *GAMESS* software with a B3LYP hybrid exchange functional and the 6-31G(*d*,*p*) basis set for all atoms in the MBB molecule (Schmidt *et al.*, 1993). No geometrical constraints were imposed during the optimization of the MBB molecule. The UV–vis spectroscopic data (oscillator strength) of the MBB molecule were computed with the time-dependent (TD-DFT) approach. Furthermore, the HOMO−1, HOMO, LUMO and LUMO+1 energy levels, their shapes, and their energy gaps were simulated using the B3LYP/6-31G(*d*,*p*) basis set.

3. Results and discussion

3.1. Single-crystal X-ray diffraction analysis

The crystallographic study of MBB was performed by an SCXRD analysis. A transparent single crystal of dimensions 0.5 × 0.5 × 0.5 mm was chosen to collect the structural information. The structure of the title compound was solved by direct methods using the *OLEX2* software and

Table 1
Crystal data and structure refinement for the MBB single crystal.

Empirical formula	$C_{15}H_{15}NO$
Formula weight	225.28
Temperature (K)	293 (2)
Crystal system	Orthorhombic
Space group	$Pna2_1$
a (Å)	9.5277 (8)
b (Å)	11.1555 (11)
c (Å)	11.7848 (10)
α (°)	90
β (°)	90
γ (°)	90
Volume (Å^3)	1252.6 (2)
Z	4
$\rho_{\rm calc}$ (g cm^{-3})	1.195
μ (mm^{-1})	0.075
F(000)	480.0
Crystal size (mm^3)	0.5 × 0.5 × 0.5
Radiation	Mo $K\alpha$ (λ = 0.71073 Å)
2θ range for data collection (°)	6.602–58.964
Index ranges	$-12 \leq h \leq 11$ $-14 \leq k \leq 14$ $-16 \leq l \leq 16$
Reflections collected	16 911
Independent reflections	3189 ($R_{\rm int}$ = 0.1078, $R_{\rm sigma}$ = 0.1256)
Data/restraints/parameters	3189/1/156
Goodness of fit on F^2	0.972
Final R indexes [$I \geq 2\sigma(I)$]	R_1 = 0.0633, wR_2 = 0.0763
Final R indexes (all data)	R_1 = 0.1902, wR_2 = 0.1079
Largest difference peak/hole (e Å^{-3})	0.12/−0.12
Flack parameter	−1.9 (10)

subsequently refined by the *SHELX97* program using the full-matrix least-squares technique (Sheldrick, 2015; Dolomanov *et al.*, 2009). The non-H atoms were refined using anisotropic displacement parameters and H atoms were treated as riding with isotropic displacement parameters. The final full-matrix least-squares refinement on F^2 with minimization of the function $\sum w(|F_o| - |F_c|)^2$ converged to R_1 = 0.0633 [for $I > 2\sigma(I)$] and wR_2 = 0.1079 (F^2, all data). The crystallographic parameters of the grown crystal with discrepancy indices are listed in Table 1. The MBB compound crystallizes in a noncentrosymmetric space group ($Pna2_1$) of an orthorhombic lattice, which is a prerequisite for nonlinear optical and piezoelectric characteristics. A displacement ellipsoid style plot of the title compound, with ellipsoids shown at the 50% probability level and H atoms shown as capped sticks for clarity, is given in Fig. 2. The crystal structure of the title compound includes intramolecular C—H···O hydrogen bonds. The –NH—(C═O)– amide group subtends dihedral angles of 19.52 (15) and 97.5 (3)° with the benzoyl ring and the *para*-substituted benzyl ring, respectively. The two aromatic rings are noncoplanar [dihedral angle = 83.65 (17)°]. These values of dihedral angles for the title crystal differ from those for several aryl amide crystals reported in the literature. The reported molecular structures of various aryl amide crystals differ in the inclination of their central amide group with respect to the benzoyl ring [dihedral angles of 19.52 (15)° for the title crystal (present work), 20.5 (1)° for *N*-(4-methylphenyl)benzamide (Gowda, Tokarčík, Kožišek & Sowmya, 2008), 59.96 (11)° for 2-methyl-*N*-(4-methylphenyl)benzamide (Gowda, Tokarčík, Kožíšek, Sowmya & Fuess, 2008) and 55.99 (7)° for 2-methyl-*N*-*p*-tolylbenzamide (Saeed *et al.*, 2010)] and in the relative orientations of the two aromatic rings [97.5 (3)° for the title crystal (present work), 63.41 (5)° for *N*-(4-methylphenyl)benzamide (Gowda, Tokarčík, Kožíšek & Sowmya, 2008), 60.9 (3)° for 2,6-dichloro-*N*-(4-methylphenyl)benzamide (Wei *et al.*, 2012), 81.44 (5)° for 2-methyl-*N*-(4-methylphenyl)benzamide (Gowda, Tokarčík, Kožíšek, Sowmya & Fuess, 2008) and 88.67 (8)° for 2-methyl-*N*-*p*-tolylbenzamide (Saeed *et al.*, 2010)].

A portion of the molecular network for the MBB compound is depicted in Fig. 3. From the figure, it is clear that MBB molecules are connected through intermolecular N—H···O hydrogen bonds, which link the molecules into infinite

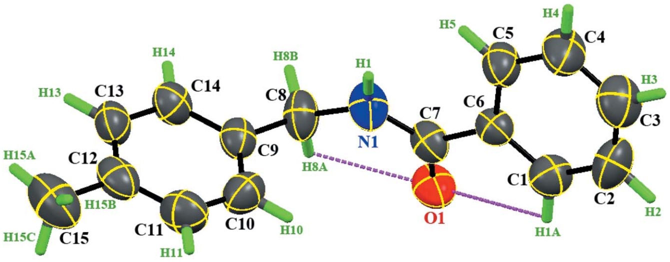

Figure 2
Displacement ellipsoid representation of the MBB compound with atomic labelling scheme. Displacement ellipsoids for non-H atoms are drawn at the 50% probability level. H atoms are represented as green-capped sticks for clarity. C, N and O atoms are displayed as dark-grey, blue and red ellipsoids, respectively.

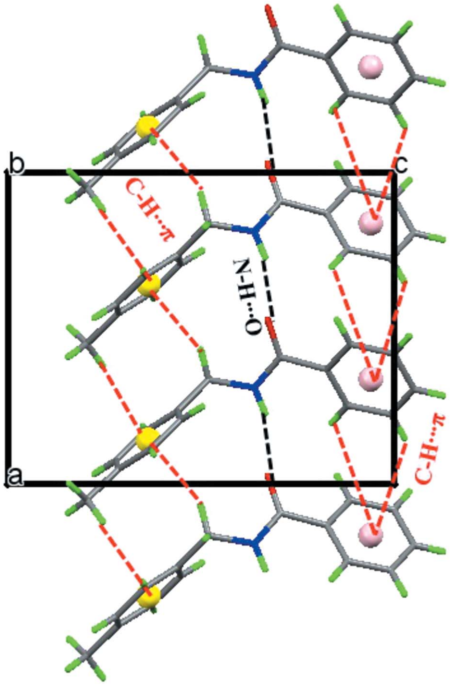

Figure 3
C—H···π interactions (red dashed lines) and N—H···O hydrogen bonds (black dashed lines) in the MBB compound, linking the molecules in head-to-head fashion along a. The yellow and pink spheres represent ring centroids.

Table 2
Experimentally observed and theoretically optimized bond lengths for MBB.

	Length (Å) (SCXRD)	Length (Å) (DFT)	Deviation (Å)
O1—C7	1.227 (5)	1.232 (6)	0.005
C6—C7	1.498 (6)	1.507 (5)	0.009
C6—C5	1.385 (6)	1.403 (5)	0.018
C6—C1	1.361 (6)	1.404 (5)	0.043
C14—C9	1.376 (6)	1.401 (6)	0.025
C14—C13	1.390 (6)	1.398 (6)	0.008
C9—C8	1.515 (6)	1.515 (5)	0.000
C9—C10	1.370 (6)	1.402 (5)	0.032
N1—C7	1.331 (5)	1.368 (6)	0.037
N1—C8	1.462 (5)	1.462 (6)	0.000
C13—C12	1.369 (6)	1.402 (5)	0.033
C5—C4	1.381 (6)	1.397 (6)	0.016
C1—C2	1.386 (6)	1.395 (5)	0.009
C10—C11	1.383 (6)	1.396 (6)	0.013
C12—C11	1.367 (6)	1.403 (6)	0.036
C12—C15	1.506 (6)	1.512 (6)	0.006
C3—C2	1.371 (6)	1.399 (6)	0.028
C3—C4	1.364 (6)	1.398 (6)	0.034

supramolecular chains running along the *a* axis. Also, the crystal structure is stabilized by weak intermolecular C—H$\cdots\pi$ interactions. From Fig. 4, we can see that there are no directional interactions present between any two supramolecular layers stacked along the *a* axis. The FTIR, ^{1}H NMR, ^{13}C NMR and HRMS spectra for the obtained MBB crystals are available as supporting information (Figs. S1–S3).

The displacement parameters and fractional atomic positions for the grown crystal are provided in CIF format in the supporting information. Tables 2 and 3 summarize the bond lengths and bond angles of the title molecule, respectively. The hydrogen-bonding geometry is summarized in Table 4.

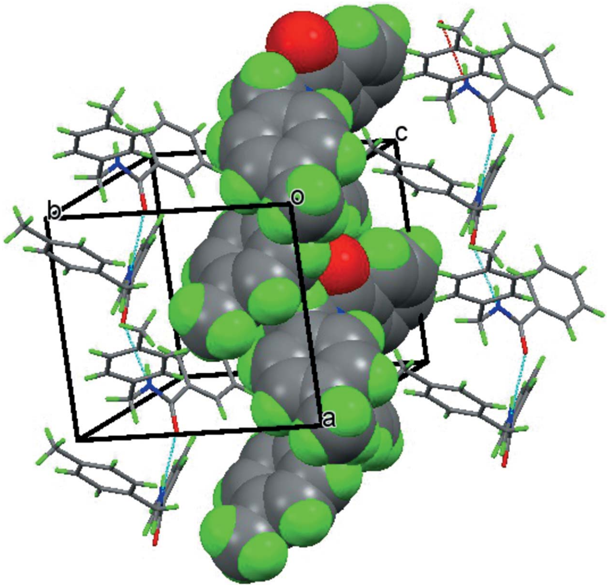

Figure 4
A molecular packing view of the MBB compound with one layer in space-filling mode. The N—H$\cdots$O hydrogen bonds are shown as blue dashed lines.

Table 3
Experimentally observed and theoretically optimized bond angles for MBB.

	Angle (°) (SCXRD)	Angle (°) (DFT)	Deviation (°)
C5—C6—C7	122.7 (5)	123.4 (6)	0.7
C1—C6—C7	119.1 (5)	117.4 (6)	−1.7
C1—C6—C5	118.2 (5)	119.2 (6)	1.0
C9—C14—C13	121.3 (5)	120.9 (6)	−0.4
C14—C9—C8	119.6 (5)	121.0 (6)	1.4
C10—C9—C14	117.8 (5)	118.2 (6)	0.4
C10—C9—C8	122.5 (5)	120.8 (6)	−1.7
C7—N1—C8	123.1 (4)	122.4 (5)	−0.7
C12—C13—C14	120.8 (5)	121.1 (6)	0.3
O1—C7—C6	119.7 (5)	121.4 (6)	1.7
O1—C7—N1	122.6 (5)	122.2 (6)	−0.4
N1—C7—C6	117.7 (4)	116.3 (6)	−1.4
C4—C5—C6	120.6 (5)	120.4 (6)	−0.2
C6—C1—C2	121.3 (5)	120.4 (6)	−0.9
N1—C8—C9	112.2 (4)	111.5 (6)	−0.7
C9—C10—C11	120.3 (5)	120.8 (6)	0.5
C13—C12—C15	121.7 (5)	120.9 (6)	−0.8
C11—C12—C13	117.4 (5)	117.8 (6)	0.4
C11—C12—C15	120.9 (6)	121.3 (6)	0.4
C12—C11—C10	122.4 (5)	121.2 (6)	−1.2
C4—C3—C2	119.2 (5)	119.8 (5)	0.6
C3—C2—C1	120.1 (5)	120.1 (5)	0.0
C3—C4—C5	120.7 (5)	120.1 (6)	−0.6

Table 4
Hydrogen-bonding parameters of MBB (Å, °).

Bond	D—H	H$\cdots A$	$D\cdots A$	D—H$\cdots A$
C5—H5$\cdots$N1$^{\rm i}$	0.930	2.617	2.894	97.82
C1—H1*A*$\cdots$O1$^{\rm i}$	0.930	2.503	2.793	98.31
C8—H8*A*$\cdots$O1$^{\rm i}$	0.970	2.395	2.795	104.15
C10—H10$\cdots$N1$^{\rm i}$	0.930	2.774	2.981	93.62
C5—H5$\cdots$O1$^{\rm ii}$	0.930	2.610	3.468	153.65
N1—H1$\cdots$O1$^{\rm ii}$	0.860	2.076	2.882	155.69
C2—H2$\cdots$O1$^{\rm iii}$	0.930	2.577	3.374	143.99

Symmetry codes: (i) x, y, z; (ii) $x + \frac{1}{2}, -y - \frac{3}{2}, z$; (iii) $-x, -y - 1, z + \frac{1}{2}$.

Table 5
Morphological importance of the MBB crystal based on the BFDH law and the HNB propagation vector theory.

Faces (hkl)	d_{hkl} (Å)	Calculated relative growth rates from BFDH law	Morphological importance by BFDH law	Relative growth rate by R_{hkl}	Morphological importance by propagation vector
(001)	11.7848	1.0000	1.0000	1.0000	1.0000
(010)	11.1555	1.0564	0.9466	4474.2729	0.0002
(100)	9.5277	1.2369	0.8085	53.2653	0.0188

3.2. Morphological studies

The correct prediction of the crystal morphology helps one to explore its efficiency and applicability in sensor and device applications (Singh *et al.*, 2012). According to the BFDH law, the growth rate of a crystal plane (hkl) is inversely dependent on its interplanar spacing (d_{hkl}) (Docherty *et al.*, 1991). On the basis of the BFDH law, Table 5 displays the relative growth rate and morphological importance (MI) of various crystal planes of the MMB crystal. Fig. 1(d) shows the indexed morphology of the MBB crystal simulated using the *WinXMorph* software (Kaminsky, 2005).

Besides the geometrical (BFDH) explanation, Hartman & Perdok (1955) proposed a theoretical model based on bond energies that successfully explains discrepancies in the BFDH law and correctly determines the crystal morphology. In HP theory, the uninterrupted periodic chains present in the crystal system are identified using information on the internal bonding present between the molecules of the crystal. These uninterrupted periodic chains of strong bonds are known as a periodic bound chain (PBC) vectors. The various faces present in the crystal system are classified into three types: F faces (flat; parallel to two or more PBC vectors), S faces (stepped; parallel to one or more PBC vector) and K faces (kinked; do not contain any PBC vectors). The order of MI associated with the occurrence of crystal faces is F > S > K. In the case of MBB crystals, the (001) plane contains the largest number (nine) of PBC vectors, which are depicted by light-blue, light-green, dark-blue, red, purple, orange, yellow, light-pink and dark-green arrows in Fig. 5. Therefore, the (001) plane belongs to the F face, which makes it the most visible in the crystal morphology. The projections of the light-green, red, light-blue, yellow and dark-green arrows are more likely to be along the (010) plane, which indicates that the (010) plane belongs to the S-face category. The (100) crystal plane also belongs to the S-face category owing to the projection of the dark-blue, purple, light-pink and orange arrows. Therefore, HP theory predicts the (001) plane of the MBB crystals to be of greater morphological importance than the other faces.

The dynamics of a rigid body are connected with its centre of mass. In our previous report, we proposed a theory (HNB vector) to predict the crystal morphology (Yadav, Sinha & Kumar, 2016). According to the HNB model, the propagation of the centre of mass of the molecular basis of a crystal system allows us to define the crystal morphology (Yadav, Sinha & Kumar, 2016). The growth rate (R_{hkl}) of the crystal plane (hkl) is defined as

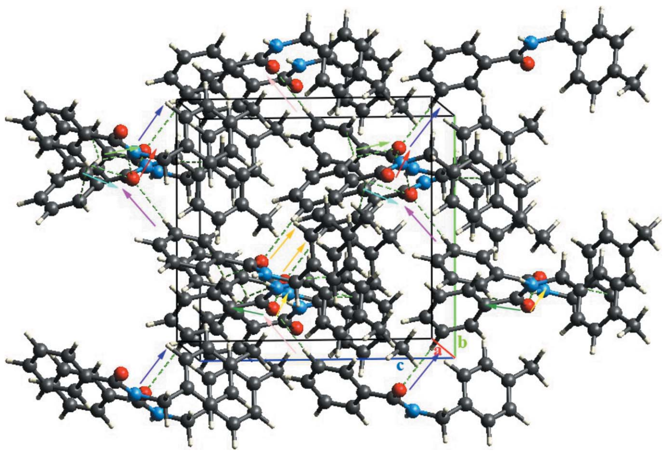

Figure 5
Molecular packing diagram of the MBB crystal along with PBC vectors. *a*, *b* and *c* denote the three crystallographic axes.

$$R_{hkl} = \frac{1}{|\mathbf{R}_{\rm P} \cdot (h\hat{i} + k\hat{j} + l\hat{k})|}, \tag{1}$$

where $\mathbf{R}_{\rm P}$ is the propagation vector of the centre of mass and h, k and l are the Miller indices of the crystal plane. Fig. 6 shows two supramolecular chains (layer 1, L1, and layer 2, L2) in the MBB crystal lattice running parallel to the a crystallographic axis. The N—H$\cdots$O, C—H$\cdots$O and O—H$\cdots$O intermolecular interactions are depicted using blue dashed lines in Fig. 6.

The arrangement of the MBB molecule is different in these two layers (L1 and L2). In layer L1 (blue ellipse), the molecular basis consists of the two MBB molecules shown in yellow (see Figs. 6 and 7). The molecular basis of layer L2 (brown ellipse) consists of the two MBB molecules shown in purple in Figs. 6 and 7. The centres of mass of molecules 1 and 2 of layer L1 are depicted by orange and green balls, respectively, in Fig. 7 and their coordinates are computed to be

$$\begin{aligned} \mathbf{r}_{11} &= 0.259989\hat{i} + 0.840827\hat{j} + 0.118092\hat{k}, \\ \mathbf{r}_{12} &= 0.759985\hat{i} + 0.659161\hat{j} + 0.122566\hat{k}. \end{aligned} \tag{2}$$

The value of the propagation vector of layer L1 is computed to be

$$\begin{aligned} \mathbf{r}_1 &= \mathbf{r}_{12} - \mathbf{r}_{11}, \\ \mathbf{r}_1 &= 0.499996\hat{i} - 0.181666\hat{j} + 0.004474\hat{k}. \end{aligned} \tag{3}$$

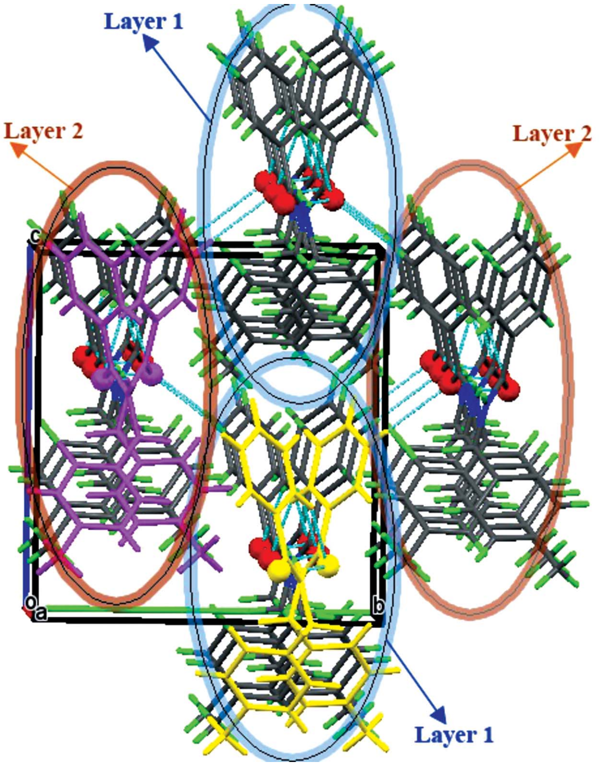

Figure 6
Packing diagram of the MBB crystal along the *a* axis. Brown and blue ellipses delimit the two supramolecular chains running parallel to the *a* axis. The molecular basis units of layers 1 and 2 are shown in yellow and purple, respectively.

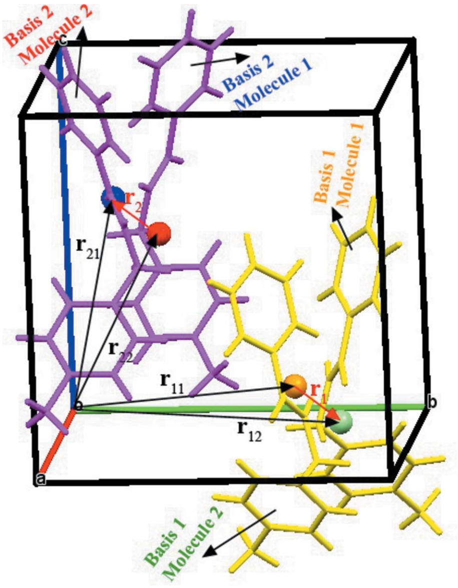

Figure 7
Unit-cell packing diagram of the MBB crystal. Calculation of propagation vector $\mathbf{R}_\mathrm{P}$ based on the centre of mass of the molecular basis.

In order to estimate the value of the propagation vector in layer L2, the same formalism as described above was used, and its value is computed to be

$$\mathbf{r}_2 = -0.500080\hat{i} + 0.181665\hat{j} + 0\hat{k}. \tag{4}$$

Finally, the resulting propagation vector is evaluated as

$$\begin{aligned} \mathbf{R}_\mathrm{P} &= \mathbf{r}_1 + \mathbf{r}_2, \\ \mathbf{R}_\mathrm{P} &= -0.84 \times 10^{-4}\hat{i} - 0.01 \times 10^{-4}\hat{j} + 44.74 \times 10^{-4}\hat{k}. \end{aligned} \tag{5}$$

Table 5 lists the relative growth rate and MI of various crystal planes of the MBB crystal based on the BFDH law and HNB propagation vector theory. The experimentally observed morphology of the MBB crystal suggests that the (001) plane is of the highest MI, which is also explained by the BFDH law, HP theory and HNB propagation vector theory.

3.3. Optimized geometry

The optimized molecular geometry of MBB was calculated by solving the self-consistent field equation for attaining true minima on the potential energy surface and is shown in Fig. 8. Tables 2 and 3 list the calculated bond length and bond angle values along with the experimental SCXRD data for the MBB compound. From Table 2, we can conclude that the C6—C1 bond has the largest deviation in bond length value (0.043 Å). Likewise, the maximum deviation in bond angle value was found as 1.7° for the C10—C9—C8, C1—C6—C7 and O1—C7—C6 bond angles (Table 3). This small discrepancy between the optimized molecular structure and its XRD counterpart may be attributed to packing interactions within the crystal lattice, which were not taken into account during computational studies.

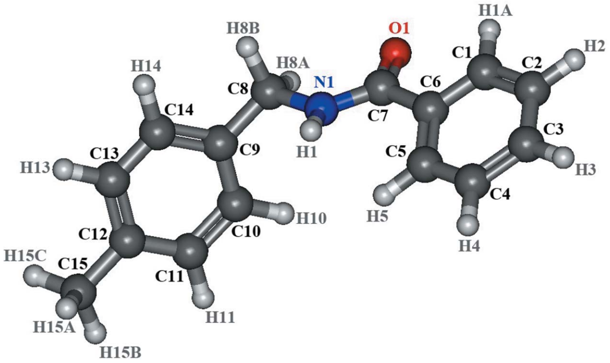

Figure 8
The theoretically optimized molecular structure of the MBB compound.

3.4. Analysis of the Hirshfeld surfaces

Hirshfeld surface analysis is a three-dimensional graphical tool which helps one understand all the intermolecular interactions present in the crystal lattice (Spackman & Byrom, 1997; Hirshfeld, 1977). The colour code information on the Hirshfeld surface provides an easy way to identify various kinds of different intermolecular interactions (Spackman & Jayatilaka, 2009). Generally, the Hirshfeld surface covers both the electron density isosurface (0.002 a.u.) and the Corey–Pauling–Koltun hard-sphere model (Yadav *et al.*, 2014). In this analysis, the structure partitioning scheme is based on dividing the crystal electron density distribution into discrete molecular fragments. The weight function for a molecular fragment of interest is defined as

$$w(r) = \rho^\mathrm{promolecule}(r)/\rho^\mathrm{procrystal}(r), \tag{6}$$

where $\rho^\mathrm{procrystal}(r)$ denotes the sum of spherical atom electron densities for the whole crystal (procrystal) and $\rho^\mathrm{promolecule}(r)$ is the same sum for a molecule (promolecule). Thus,

$$w(r) = \sum_{i \in \mathrm{molecule}\ A} \rho_i(r) \Big/ \sum_{i \in \mathrm{crystal}} \rho_i(r), \tag{7}$$

where $\rho_i(r)$ is the spherically averaged atomic electron charge density located at the ith nucleus (Yadav, Sinha, Goel *et al.*, 2016; Spackman & Byrom, 1997). The weight function $w(r)$ is a continuous function and its value lies in the range $0 < w(r) < 1$. The molecular surfaces are generated across the molecule by integrating over the weighted electron density, $w(r)\rho(r)$. The isosurface which is constructed by considering $w(r) = 0.5$ and covers the 0.002 a.u. electron density isosurface is known as the Hirshfeld surface.

d_i and d_e represent the contact distances of nearest atoms inside and outside, respectively, the Hirshfeld surface. In order to enable both donor and acceptor interactions on the same molecular Hirshfeld surface, the concept of normalized contact distance (d_norm) was incorporated (McKinnon *et al.*, 2007). d_norm is expressed as a function of d_i, d_e and the van der Waals (vdW) radii of atoms as follows:

$$d_\mathrm{norm} = \frac{d_\mathrm{i} - r_\mathrm{i}^\mathrm{vdW}}{r_\mathrm{i}^\mathrm{vdW}} + \frac{d_\mathrm{e} - r_\mathrm{e}^\mathrm{vdW}}{r_\mathrm{e}^\mathrm{vdW}}, \tag{8}$$

where $r_{\rm e}^{\rm vdW}$ and $r_{\rm i}^{\rm vdW}$ denote the vdW radii of atoms external and internal to the molecular surface, respectively. A specific colour code is chosen to represent the intermolecular contacts on the molecular Hirshfeld surface as follows: red for vdW < $d_{\rm norm}$, blue for vdW > $d_{\rm norm}$ and white for intermediate distance. In this fixed colour scale scheme, the $d_{\rm norm}$ value is 0.0 for white, 1.10 (positive) for blue and −0.75 (negative) for red.

Figs. 9 and 10 represent two different views of the Hirshfeld surface mapped over $d_{\rm norm}$ for the MBB crystal along with close contacts with the neighbouring molecules. In each figure, the bright-red spot on the Hirshfeld surface appearing near carbonyl oxygen O1 and amine hydrogen H1 represents the acceptor and donor of the dominating N—H···O hydrogen bonds. These are seen as red and blue regions in the Hirshfeld surface mapped over electrostatic potential in Fig. 11 and correspond to negative and positive potentials, respectively. The other four faint red spots in Figs. 9 and 10 are due to the presence of comparatively weak C—H···O interactions. The blue region on the Hirshfeld surface depicts the comparatively weak intermolecular interactions like H···H.

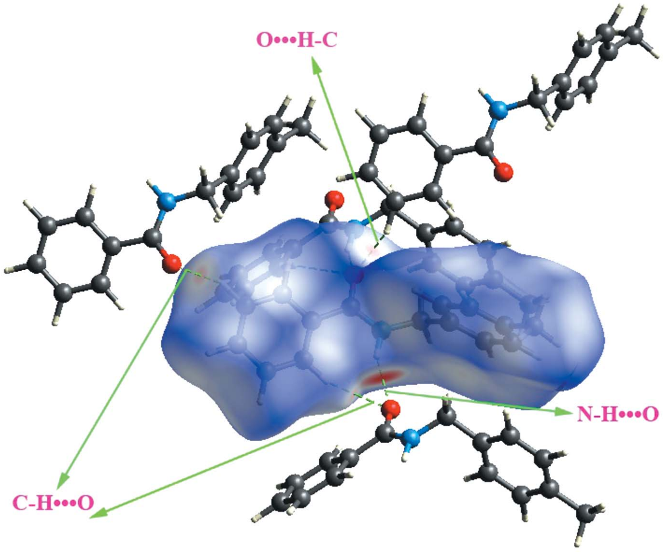

Figure 9
A view of the Hirshfeld surface mapped over $d_{\rm norm}$, depicting N—H···O and C—H···O interactions of the MBB molecule with its immediate environment.

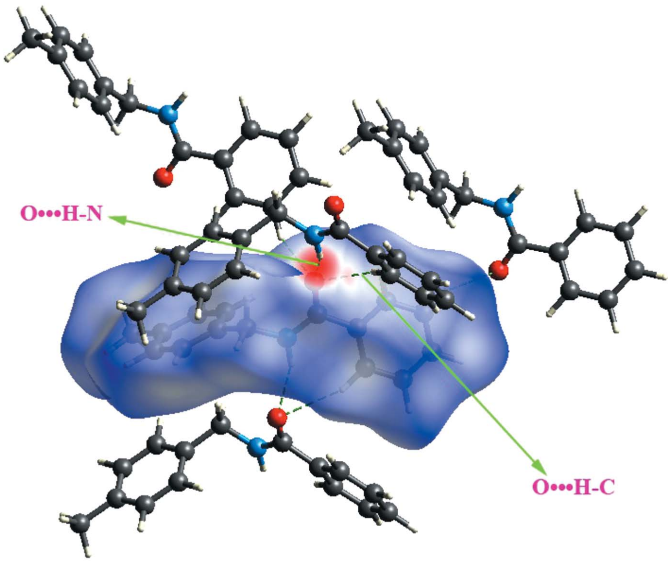

Figure 10
A different view of the Hirshfeld surface mapped over $d_{\rm norm}$.

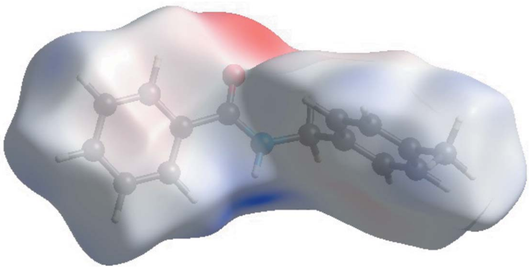

Figure 11
A view of the Hirshfeld surface mapped over the electrostatic potential.

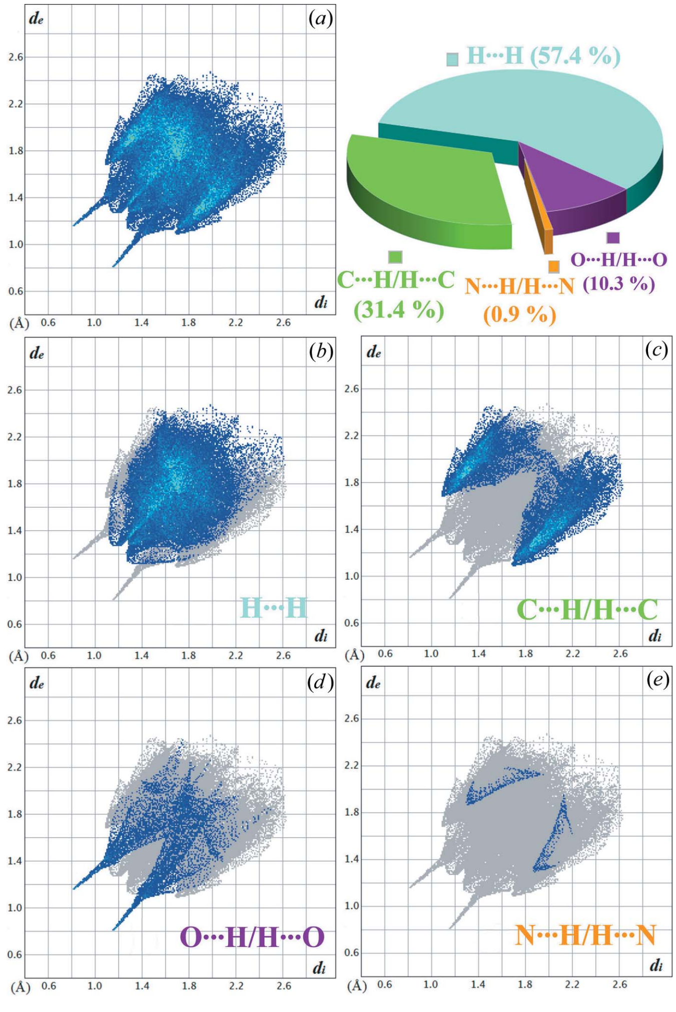

Figure 12
(*a*) A two-dimensional fingerprint plot depicting all the intermolecular interactions present in the MBB crystal structure. (*b*)–(*e*) The individual contributions from different contacts to the Hirshfeld surface of the title compound.

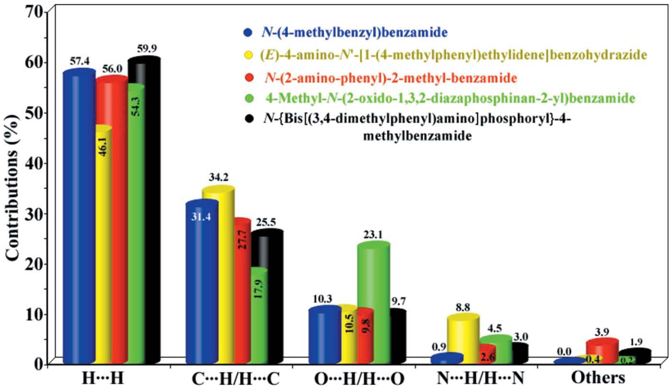

Figure 13

Relative contributions of various intermolecular contacts for several aryl amide crystals. (1) *N*-(4-Methylbenzyl)benzamide (present work), (2) (*E*)-4-amino-*N*′-[1-(4-methylphenyl)ethylidene]benzohydrazide (Sivajeyanthi *et al.*, 2017), (3) *N*-(2-aminophenyl)-2-methylbenzamide (Nagaraju *et al.*, 2016), (4) 4-methyl-*N*-(2-oxido-1,3,2-diazaphosphinan-2-yl)benzamide (Saneei *et al.*, 2017) and (5) *N*-{bis[(3,4-dimethylphenyl)amino]phosphoryl}-4-methylbenzamide (Saneei *et al.*, 2017).

A fingerprint plot of d_e *versus* d_i (Spackman & McKinnon, 2002) provides a convenient two-dimensional summary of the intermolecular interactions in the crystal system. Fig. 12(*a*) displays the two-dimensional fingerprint plot for the title molecule. It involves all the intermolecular interactions present within the grown crystal structure. The overall two-dimensional fingerprint plot is decomposed into H$\cdots$H, C$\cdots$H/H$\cdots$C, O$\cdots$H/H$\cdots$O and N$\cdots$H/H$\cdots$N to quantify their relative contributions within the structure (Figs. 12*b*–12*e*). Fig. 12(*b*) shows that the H$\cdots$H interactions make the most significant contribution (57.4%) to the Hirshfeld surface. These interactions play an important role in the molecular packing of the MBB crystal. The 31.4% contribution from C$\cdots$H/H$\cdots$C contacts (Fig. 12*c*) is due to the presence of short C—H$\cdots\pi$ intermolecular interactions. In the packing of the molecular crystal, C—H$\cdots\pi$ interactions play an important role and can affect the optical properties. The pair of long spikes with tips at $d_e + d_i \simeq 1.95$ Å in Fig. 12(*c*) are the result of short interatomic N—H$\cdots$O contacts (Table 4). This significant contribution from O$\cdots$H/H$\cdots$O contacts (10.3%) to the Hirshfeld surface is also due to the presence of C—H$\cdots$O and N—H$\cdots$O hydrogen bonds. These interactions decide the electric properties of the crystal, such as dielectric constant, piezoelectricity *etc.* Hence, the structural geometry of the crystal is connected to its physical properties and also indicates the potential future role of the material in various related applications. The relative contributions of various intermolecular contacts for several aryl amide crystals reported in the literature are compared in a bar chart in Fig. 13.

The local shape efficiency of three-dimensional Hirshfeld surfaces can be assessed by using tools that measure surface curvature such as the shape index and curvedness map. The shape index (S) is a function of the principal curvatures ($k_{\max}$ and $k_{\min}$) and is expressed as (Roberts, 2001)

$$S = \frac{2}{\pi}\arctan\left(\frac{k_{\max} + k_{\min}}{k_{\max} - k_{\min}}\right). \tag{9}$$

The map of the shape index on the Hirshfeld surface can be used to represent the local morphology in terms of colour-coded information, *i.e.* complementary bumps (blue) and hollow regions (red). It provides a visual identification of the regions where two molecular Hirshfeld surfaces touch one another. Fig. 14(*a*) illustrates the front and rear sides of the molecular Hirshfeld surface of the title molecule mapped over shape index. The bright red sites identified with arrows 1, 2 and 3 indicate the C$\cdots$H, O$\cdots$H and H$\cdots$H interactions, respectively.

The map of curvedness (C) gives a measure of the total curvature present within the surface and is defined by

$$C = \frac{2}{\pi}\ln\left(\frac{k_{\max}^2 + k_{\min}^2}{2}\right)^{1/2}. \tag{10}$$

The magnitude of C depends on the value of r.ms. curvature of the surface and on the length scale (McKinnon *et al.*, 2004; Inan & Halici, 2012). Maps of C are typically characterized by large flat regions of green colour separated by blue edges. From Fig. 14(*b*), we see that small segments of flat green regions are delineated by blue outlines, confirming the absence of π–π stacking interactions. This is also evident from the fact that there is zero contribution from C$\cdots$C contacts to the Hirshfeld surface (see Fig. 12).

The porous properties of crystalline materials play a considerable role in deciding various anisotropic properties of single crystals. Void mapping for the as-grown crystals was performed to visualize and locate the void space present in the

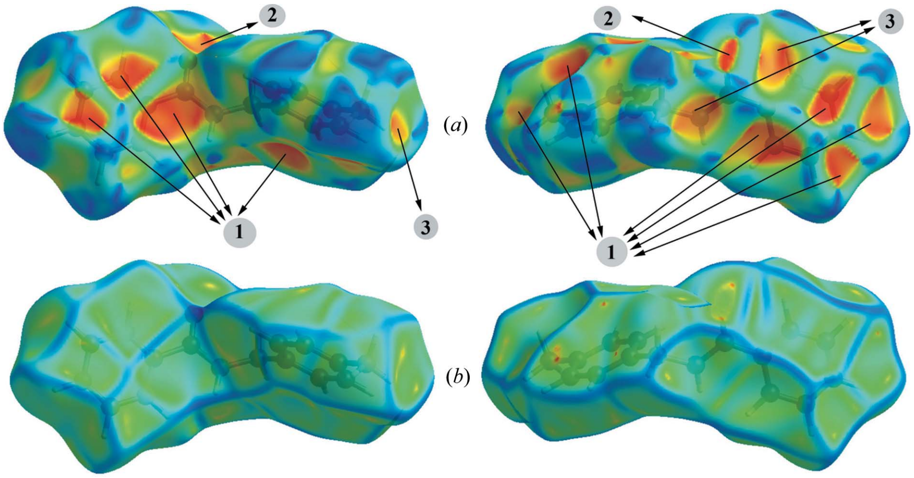

Figure 14

(*a*) Hirshfeld surfaces of the MBB molecule with shape index mapped onto the surface. Blue and red regions denote bumps and hollow regions, respectively. (*b*) Hirshfeld surfaces with curvedness mapped onto the surface to recognize the curved and planar regions in the MBB molecule.

crystal lattice and to compute volumes and surface areas of void space and porosity (Turner *et al.*, 2011). Fig. S4 in the supporting information displays the unit-cell packing diagram of the MBB compound with voids mapped at the 0.002 a.u. isosurface along the crystallographic *a* axis. The void channels were found to occupy 13.5% of the unit-cell volume with a surface area of 547.57 Å^2. From void analysis, we can conclude that cavity channels are uniformly distributed in the crystal lattice, which shows the scope of binding of the title compound with metal ions to alter its physical properties.

Table 6
The calculated quantum molecular descriptors of the MBB molecule.

Properties	b3lyp/6-311g**
$E_{\rm HOMO}$ (eV)	−6.5144
$E_{\rm LUMO}$ (eV)	−1.2001
Energy band gap $\lvert E_{\rm HOMO} - E_{\rm LUMO}\rvert$ (eV)	5.314
Electron affinity ($I = -E_{\rm HOMO}$) (eV)	6.514
Electron affinity ($A = -E_{\rm LUMO}$) (eV)	1.200
Chemical hardness [$\eta = (I - A)/2$] (eV)	2.657
Electronegativity [$\chi = (I + A)/2$] (eV)	3.857
Chemical potential [$\mu = -(I + A)/2$] (eV)	−3.857
Softness ($\zeta = 1/2\eta$) (eV^{-1})	0.188
Electrophilicity index ($\omega = \chi^2/2\eta$) (eV)	2.799

3.5. UV–vis–NIR spectral and HOMO–LUMO analysis

Fig. 15(*a*) illustrates the experimental UV–vis–NIR absorbance spectrum of an MBB crystal in the wavelength range from 200 to 800 nm. The grown crystal was observed to exhibit minimum optical absorbance in the visible region and the cutoff wavelength was found to be at 260 nm. This absorption band observed at 260 nm can be assigned to n–π^* transitions and to excitation in the C═O group and the aromatic rings (Crasta *et al.*, 2004). Intriguingly, we observed from the absorbance spectrum that the title crystal does not absorb light in the region between 300 and 800 nm, which makes it a potential candidate for optical window applications. The simulated UV–vis spectrum of the MBB crystal was evaluated by the TD-DFT method and is displayed in Fig. 15(*b*). The theoretically calculated value of the strong absorption peak was computed as 248 nm/5.01 eV/0.102 (wavelength/excitation energy/oscillator strength), which agrees well with the experimental value.

The optical band gap of the grown crystal was estimated using Tauc's relation: $(\alpha h\nu)^n = A(h\nu - E_g)$, where ν represents the incident frequency, h denotes Planck's constant, E_g is the band gap, A is a constant independent of photon energy, n determines the nature of electronic transitions (n = 1/2 for indirect allowed transitions and n = 2 for allowed direct transitions) and α is the absorption coefficient measured in cm^{-1} (Tauc & Menth, 1972). Its value was calculated using the expression $\alpha = \ln(1/T)/t$, where T is the transmittance and t is the thickness of the specimen. In the Tauc plot [see inset of Fig. 15(*a*)], the value of the energy band gap can be obtained from the intersection point of the extrapolated linear portion

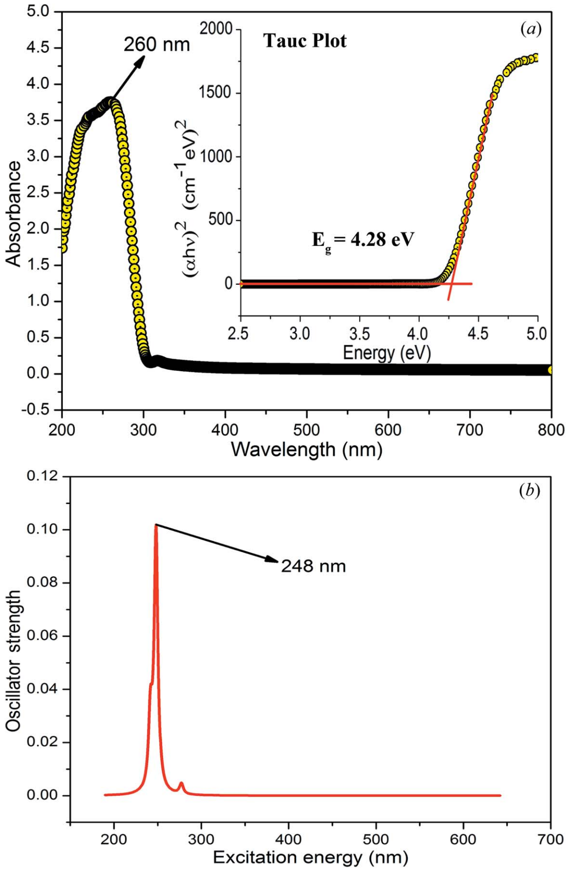

Figure 15
The (*a*) experimental and (*b*) simulated UV–vis–NIR spectra of the MBB crystal. The inset shows the Tauc plot of $(\alpha h\nu)^2$ against $h\nu$; the value of the direct optical band gap is equal to 4.28 eV.

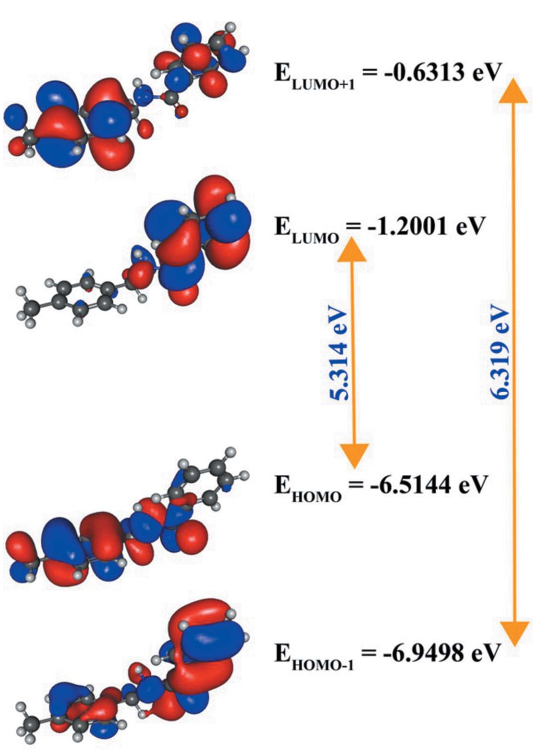

Figure 16
The HOMO−1, HOMO, LUMO and LUMO+1 energy levels, their shapes, and the energy gaps of the MBB molecule.

of the absorption edge with the energy ($h\nu$) axis. The value of E_g was calculated to be 4.28 eV. The low cutoff wavelength and large optical transmittance window confirm the absence of grain boundaries and the presence of low defect concentrations in the crystal lattice (Weber, 2003). This behaviour indicates the potential utility of MBB in the upgrade and design of various optoelectronic applications. Zedan *et al.* (2015) have reported a band gap of 2.9 eV for *N*-{5-[(antipyrinylhydrazono)cyanomethyl][1,3,4]thiadiazol-2-yl}benzamide.

In quantum chemistry, both the molecular orbitals (LUMO and HOMO) and their energy gap (E_g) are very useful parameters in determining the intermolecular charge transfer interactions in the molecule and its chemical stability. In the case of the MBB crystals, the distributions of the LUMO+1, LUMO, HOMO and HOMO−1 energy levels, their shapes, and their energy gaps were computed using the B3LYP/6-311G** basis set in the *GAMESS* program (Schmidt *et al.*, 1993) and are depicted in Fig. 16. In the MBB molecule, the HOMO is localized on the *para*-substituted benzyl ring and the –NH—(C═O)– amide group, while the LUMO is entirely located on the benzoyl ring. The HOMO–LUMO energy band gap (ΔE = LUMO − HOMO) of the MBB molecule is estimated to be 5.31 eV and is used to determine the values of the various quantum molecular descriptors summarized in Table 6. The optical band gap of the MBB crystal was evaluated from the experimental UV–vis analysis to be equal to 4.28 eV, which is in agreement with the theoretically predicted value from LUMO–HOMO analysis (5.31 eV).

3.6. Photoluminescence studies

Generally, pure organic crystals belong to the category of non-phosphorescent material. However, bright phosphorescence is also observed from the organic matrix because of features like aromatic carbonyls, halogen bonding and the heavy-atom effect (Bolton *et al.*, 2011). In organic materials, the generation of only singlet excitons is favoured by electronic dipole transitions. In order to excite triplet excitons, strong exciton spin-orbit interaction is needed to flip the spin of the triplet configuration in the excited state of the molecule (Ompong & Singh, 2016). In the case of aromatic carbonyls, spin-orbit coupling exhibited at the carbonyl O atom allows intrinsic triplet generation through intersystem crossing (Bolton *et al.*, 2011). Fig. 17 shows the PL spectrum of an MBB crystal at room temperature. Broad emission was observed in the region of 350–450 nm at an excitation of 290 nm. Luminescence spectra are generally blurred and diffuse at room temperature and this may be attributed to variation in the strength of the crystalline field occurring from thermal disturbances (Pant, 1943). A second possible cause is a high contribution from weak intermolecular interactions present in the grown crystal system, which leads to sheer congestion: the rovibronic transitions may be too numerous to separate (Byrne & Ross, 1965). On the spectral deconvolution of a main broad peak, three emission bands were identified at 347,

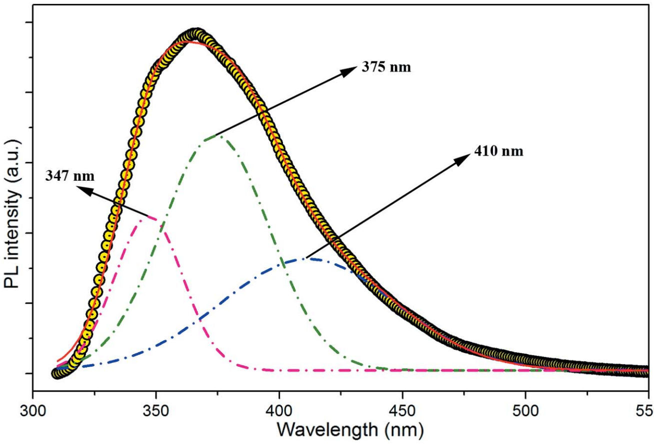

Figure 17
PL emission spectrum of the MBB crystal at an excitation of 290 nm. Three broad emission peaks were found at 347, 375 and 410 nm.

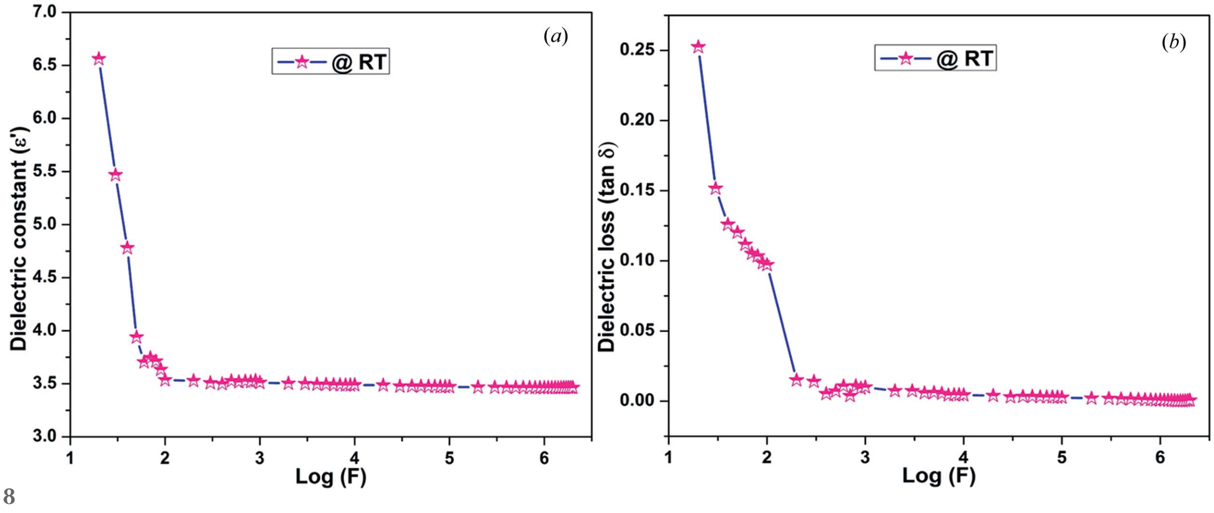

Figure 18
(*a*) Plot of dielectric constant *versus* log (F) at room temperature (RT) for the MBB crystal. (*b*) Plot of dielectric loss with log (F) at room temperature for the MBB crystal.

375 and 410 nm (UV and blue regions). Thus, the MBB crystal becomes a potential candidate for radiation detector and laser applications.

3.7. Dielectric studies

Fig. 18(*a*) shows the variation of the dielectric constant with frequency at room temperature for the MBB crystal. It was observed that the value of the dielectric constant suddenly decreased from 6.5 to 3.5 in the low-frequency region of 20–100 Hz. Owing to the effect of all four polarizations (space charge, orientational, electronic and ionic) at low frequency, the value of the resulting dielectric constant becomes high. However, the value of the dielectric constant attains a constant value of ~3.5 in the high-frequency region (100 Hz–2 MHz). A possible consequence of the constant value of dielectric constant is the progressive loss of significance of various polarizations in the higher-frequency region. Fig. 18(*b*) shows a plot of dielectric loss against frequency at room temperature. Initially, at lower frequencies, the value of the dielectric loss was found to be 0.25. Subsequently, in the high-frequency region, the value of dielectric loss becomes $\tan\delta = 0.002$, which indicates that there are few defects and the title compound has a highly crystalline nature. Moreover, the low dielectric loss at higher frequency in the grown crystal is directly related to the optical quality of the crystal with fewer grain boundaries.

3.8. Piezoelectricity

Piezoelectric crystals can convert mechanical vibrations and movements into electric charge and *vice versa*. In organic crystals, the collective responses of hydrogen bonds and $\mathrm{C—H}\cdots\pi$ interactions to the applied electric field decide the piezoelectric behaviour of the grown crystal. For the design of highly piezoelectric organic materials, both the dipole moment and the polarizability of hydrogen-bonded systems need to be considered carefully (Gagrai *et al.*, 2016). In hydrogen-bonding systems, a bond or vibration mode with low force constant and a large change in dipole moment with a change in bond length are required for a large piezoelectric effect (Werling *et al.*, 2014). The value of the piezoelectric coefficient on the (001) face of the MBB crystal was found to be 15 pC N^{-1}. The promising piezoelectric nature of the MBB crystal makes it useful for energy-harvesting, sensor and actuator applications.

3.9. Vickers micro-hardness testing

The micro-hardness of the MBB crystal was determined using the Vickers micro-hardness technique. Here, the dimensions of the impression resulting from the penetration of an indenter are monitored under constant applied load. The indenter load was varied from 5 to 40 g for static indentation with a fixed dwell time of 5 s. The Vickers hardness number (VHN) is expressed as (Lopez, 1993) $H_\mathrm{v} = (1.8544P/d^2)$ N m^{-2}, where P is the applied indenter load in N, d is the average diagonal length of indentation in m and 1.8544 is a constant geometrical factor for the diamond pyramid indenter. Fig. 19(*a*) shows the variation of VHN against indenter load and also displays the indentation marks at various applied loads on the MBB crystal plane. Initially, the micro-hardness value increases with indenter load up to 20 g, because at low values of applied load only the top surface layers of the crystal are pierced. This variation in hardness number reflects the reverse indentation size effect (RISE) (Goel *et al.*, 2016). The maximum value of the VHN was computed to be 1.5×10^6 N m^{-2} for a 20 g indenter load. Beyond 20 g, the value of VHN starts to decrease and it attains a constant value (1.0×10^6 N m^{-2}) after 50 g. This type of nonlinear decrease in hardness with indenter load is due to release of stress generated in the form of cracks. This variation in hardness number shows the normal indentation size effect (ISE).

Mayer's law is used to understand the variation of load and is defined as (Iurchenko *et al.*, 2016) $P = Ad^n$, where A is the material constant and n is called Meyer's index. The value of n can be estimated from a logarithmic plot of $\ln(p)$ against $\ln(d)$ (Fig. 19*b*). The computed value of n (1.88) was observed to be

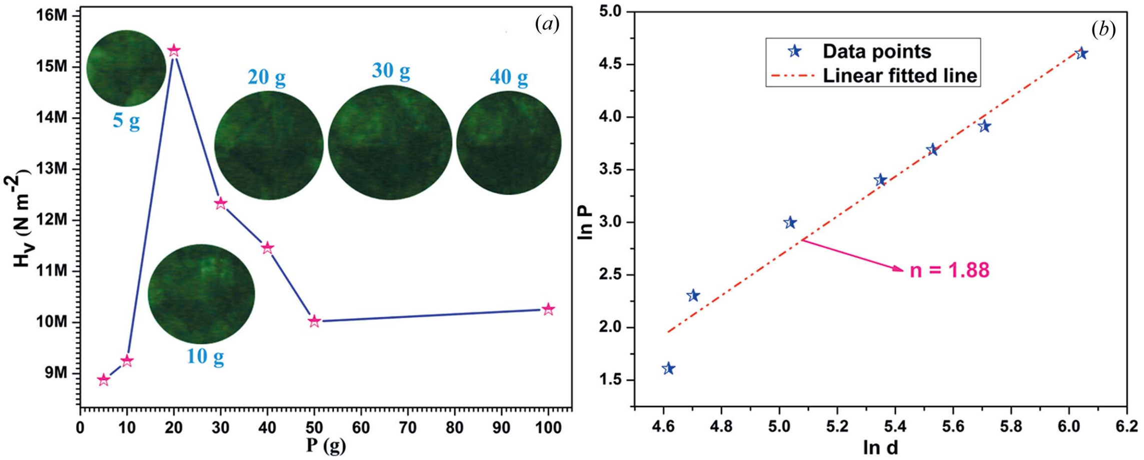

Figure 19
(*a*) Plot of H_v *versus* indenter load (P) for the MBB crystal and photographs of the indentation marks at various loads (5, 10, 20, 30 and 40 g) on the crystal plane (001). (*b*) The variation of $\ln(P)$ against $\ln(d)$ for Meyer's index evaluation.

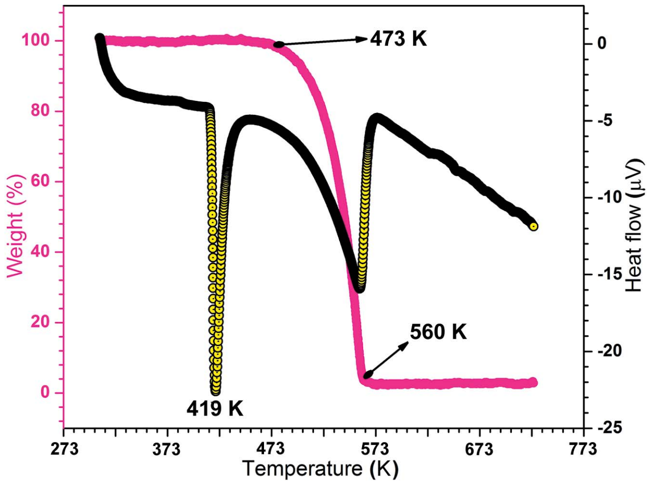

Figure 20
TG/DTA curves of the MBB single crystal.

greater than 1.6, which suggests the softer nature of the grown crystals.

3.10. Thermal analysis

Thermogravimetric and differential thermal analysis are useful tools which help in obtaining information about the thermal stability and melting point of a material. The TG/DTA measurements were conducted on an MBB crystal at a heating rate of 10 K min^{-1} under nitrogen atmosphere. Fig. 20 displays the TG spectrum recorded in the temperature range 308–723 K for the MBB crystal. The results clearly show that there is no weight loss up to 473 K, indicating that the MBB crystal is thermally stable in the temperature range of room temperature to 473 K, which further emphasizes its potential use for optoelectronic devices at higher temperatures. Above 473–560 K, 97% of the MBB material decomposes. In the DTA curve of the MBB crystal (see Fig. 20), there occurs an endothermic peak (melting point) at 419 K.

4. Conclusion

In summary, *N*-(4-methylbenzyl)benzamide was synthesized using a simple and versatile approach. The slow evaporation method was used to harvest single crystals of the synthesized material. SCXRD analysis on a selected crystal confirms that the it belongs to the orthorhombic space group $Pna2_1$. The two aromatic rings are almost perpendicular to each other, forming a dihedral angle of 83.65 (17)°. The crystal packing of the MBB crystal shows that the high propensity for formation of N—H···O hydrogen bonds and C—H···π interactions leads to infinite supramolecular chains running parallel to the *a* axis. The geometrical considerations of the HNB propagation vector of centre of mass explain the morphological importance of the most visible (001) crystal plane, which is in agreement with the results of other existing theoretical models. An analysis of the molecular Hirshfeld surface provided a summary of all the intermolecular contacts in the crystal. Also, molecular Hirshfeld surface analysis depicted the immediate environment of the molecule in the crystal packing and identified the close contacts between neighbouring molecules. The relative contributions from H···H, C···H/H···C, O···H/H···O and N···H/H···N interactions were found to be 57.4, 31.4, 10.3 and 0.9%, respectively. The significant contributions from C···H/H···C and O···H/H···O contacts confirm the presence of C—H···π interactions and C—H···O and N—H···O hydrogen bonds, respectively. The topology of the three-dimensional molecular surface was analysed using the shape index and curvedness mapping. A void analysis study shows that the MBB crystal possesses uniformly distributed void channels, which contribute further scope for tailoring its anisotropic properties. The FTIR, NMR and HRMS analyses confirm the presence of all the functional groups that contribute to the molecular structure of the grown crystals. The UV–vis analysis results showed that the crystal exhibits a lower cutoff wavelength of 285 nm and E_g = 4.28 eV, which makes the MBB crystal a promising and competitive candidate for future optoelectronic devices. The PL emission spectrum shows UV and blue richness (347, 375 and 410 nm) for the MBB crystal, which makes it applicable for laser and photonic devices. The MBB crystal has shown potential for microelectronic and piezoelectric applications, with a low value of dielectric constant (~3.5) and high value of the piezo-coefficient (15 pC N^{-1}). A Vickers micro-hardness study revealed the softer nature of the grown crystals. The melting point of the MBB crystal was found to be 419 K and the compound was thermally stable up to 473 K. The optimized molecular geometry, UV–vis spectrum and HOMO–LUMO energy gap for the MBB molecule were found to be consistent with experimental results.

Acknowledgements

HY and SG would like to thank UGC and CSIR for scholarships. NS expresses her gratitude to the Principal, SGTB Khalsa College.

Funding information

The following funding is acknowledged: Armament Research Board, DRDO (award No. ARMREB/MAA/ 2015/163); SERB, DST (award No. EMR/2015/000385). BS would like to express his personal thanks to Fundação para a Ciência e a Tecnologia for postdoctoral research grant SFRH/BPD/76184/2011. IB wishes to acknowledge the Portuguese Foundation for Science and Technology for financial support (grant IF/00582/2015).

References

Bolton, O., Lee, K., Kim, H.-J., Lin, K. Y. & Kim, J. (2011). *Nat. Chem.* **3**, 207–212.
Bowes, K. F., Glidewell, C., Low, J. N., Skakle, J. M. S. & Wardell, J. L. (2003). *Acta Cryst.* C**59**, o1–o3.
Brooks, J. S. (2010). *Chem. Soc. Rev.* **39**, 2667–2694.

Bülbül, H., Köysal, Y., Dege, N., Gümüş, S. & Ağar, E. (2015). *J. Crystallogr.* **2015**, 1–6.

Byrne, J. P. & Ross, I. G. (1965). *Can. J. Chem.* **43**, 3253–3257.

Crasta, V., Ravindrachary, V., Bhajantri, R. F. & Gonsalves, R. (2004). *J. Cryst. Growth*, **267**, 129–133.

Docherty, R., Clydesdale, G., Roberts, K. J. & Bennema, P. (1991). *J. Phys. D Appl. Phys.* **24**, 89–99.

Dolomanov, O. V., Bourhis, L. J., Gildea, R. J., Howard, J. A. K. & Puschmann, H. (2009). *J. Appl. Cryst.* **42**, 339–341.

Durgaiah, C., Naresh, M., Swamy, P., Srujana, K., Rammurthy, B. & Narender, N. (2016). *Catal. Commun.* **81**, 29–32.

Elbagerma, M. A., Edwards, H. G. M., Munshi, T. & Scowen, I. J. (2010). *Anal. Bioanal. Chem.* **397**, 137–146.

Gagrai, A. A., Mundlapati, V. R., Sahoo, D. K., Satapathy, H. & Biswal, H. S. (2016). *ChemistrySelect*, **1**, 4326–4331.

Goel, S., Sinha, N., Yadav, H., Hussain, A. & Kumar, B. (2016). *Mater. Res. Bull.* **83**, 77–87.

Gowda, B. T., Tokarčík, M., Kožíšek, J. & Sowmya, B. P. (2008). *Acta Cryst.* E**64**, o83.

Gowda, B. T., Tokarčík, M., Kožíšek, J., Sowmya, B. P. & Fuess, H. (2008). *Acta Cryst.* E**64**, o1494.

Gundlach, D. J. (2007). *Nat. Mater.* **6**, 173–174.

Haffner, C. D., Thomson, S. A., Guo, Y., Petrov, K., Larkin, A., Banker, P., Schaaf, G., Dickerson, S., Gobel, J., Gillie, D., Condreay, J. P., Poole, C., Carpenter, T. & Ulrich, J. (2010). *Bioorg. Med. Chem. Lett.* **20**, 6989–6992.

Haffner, C. D., Thomson, S. A., Guo, Y., Schaller, L. T., Boggs, S., Dickerson, S., Gobel, J., Gillie, D. & Condreay, J. P. (2010). *Bioorg. Med. Chem. Lett.* **20**, 6983–6988.

Han, K.-J. & Kim, M. (2014). *Org. Prep. Proced. Int.* **46**, 370–375.

Hartman, P. & Perdok, W. G. (1955). *Acta Cryst.* **8**, 49–52.

Hirshfeld, F. L. (1977). *Theor. Chim. Acta*, **44**, 129–138.

Inan, T. & Halici, U. (2012). *IEEE Trans. Inf. Forensics Secur.* **7**, 577–587.

Iurchenko, A., Borc, J., Sangwal, K. & Voronov, A. (2016). *Mater. Chem. Phys.* **170**, 276–284.

Kaminsky, W. (2005). *J. Appl. Cryst.* **38**, 566–567.

Karabulut, H. R. F. & Kacan, M. (2002). *Synth. Commun.* **32**, 2345–2348.

Kerdphon, S., Quan, X., Parihar, V. S. & Andersson, P. G. (2015). *J. Org. Chem.* **80**, 11529–11537.

Kippelen, B. & Brédas, J.-L. (2009). *Energ. Environ. Sci.* **2**, 251.

Klauk, H., Zschieschang, U., Pflaum, J. & Halik, M. (2007). *Nature*, **445**, 745–748.

Lopez, J. (1993). *Polym. Test.* **12**, 437–458.

Luo, J. T. & Huangn, W. Q. (2004). *Jiegou Huaxue*, **23**, 320–323.

McKinnon, J. J., Jayatilaka, D. & Spackman, M. A. (2007). *Chem. Commun.* **2007**, 3814–3816.

McKinnon, J. J., Spackman, M. A. & Mitchell, A. S. (2004). *Acta Cryst.* B**60**, 627–668.

Nagaraju, L. R., Venkataravanappa, L. R., Mandayam Anandalwar, S. & Khanum, S. A. (2016). *J. Appl. Chem.* **2016**, 1–7.

Nageswara Rao, S., Chandra Mohan, D. & Adimurthy, S. (2014). *Green Chem.* **16**, 4122–4126.

Nammalwar, B., Muddala, N. P., Watts, F. M. & Bunce, R. A. (2015). *Tetrahedron*, **71**, 9101–9111.

Ompong, D. & Singh, J. (2016). *Phys. Status Solidi (C)*, **13**, 89–92.

Pant, D. D. (1943). *Proc. Indian Acad. Sci. Sect. A*, **18**, 309–326.

Revathi, B. K., Reuben Jonathan, D., Sathya, S., Prathebha, K. & Usha, G. (2015). *Acta Cryst.* E**71**, o359–o360.

Roberts, A. (2001). *First Break*, **19**, 85–100.

Saeed, A., Khera, R. A. & Simpson, J. (2010). *Acta Cryst.* E**66**, o911–o912.

Saha, B., Sengupta, G., Sarbajna, A., Dutta, I. & Bera, J. K. (2014). *J. Organomet. Chem.* **771**, 124–130.

Saneei, A., Pourayoubi, M., Jenny, T. A., Crochet, A., Fromm, K. M. & Shchegravina, E. S. (2017). *Chem. Pap.* https://doi.org/10.1007/s11696-017-0168-x.

Schmidt, M. W., Baldridge, K. K., Boatz, J. A., Elbert, S. T., Gordon, M. S., Jensen, J. H., Koseki, S., Matsunaga, N., Nguyen, K. A., Su, S., Windus, T. L., Dupuis, M. & Montgomery, J. A. (1993). *J. Comput. Chem.* **14**, 1347–1363.

Sheldrick, G. M. (2015). *Acta Cryst.* C**71**, 3–8.

Shen, X.-X., Liu, Q., Xing, R.-G. & Zhou, B. (2008). *Catal. Lett.* **126**, 361–366.

Singh, M. R., Chakraborty, J., Nere, N., Tung, H.-H., Bordawekar, S. & Ramkrishna, D. (2012). *Cryst. Growth Des.* **12**, 3735–3748.

Sivajeyanthi, P., Jeevaraj, M., Edison, B. & Balasubramani, K. (2017). *Acta Cryst.* E**73**, 1029–1032.

Spackman, M. A. & Byrom, P. G. (1997). *Chem. Phys. Lett.* **267**, 215–220.

Spackman, M. A. & Jayatilaka, D. (2009). *CrystEngComm*, **11**, 19–32.

Spackman, M. A. & McKinnon, J. J. (2002). *CrystEngComm*, **4**, 378–392.

Spackman, M. A., McKinnon, J. J. & Jayatilaka, D. (2008). *CrystEngComm*, **10**, 368–376.

Tauc, J. & Menth, A. (1972). *J. Non-Cryst. Solids*, **8–10**, 569–585.

Turner, M. J., McKinnon, J. J., Jayatilaka, D. & Spackman, M. A. (2011). *CrystEngComm*, **13**, 1804–1813.

Weber, M. J. (2003). *Handbook of Optical Materials.* New York: CRC Press.

Wei, P.-F., Hao, L.-Y., Yang, X.-L., Ye, Y.-F. & Feng, Z.-Q. (2012). *Acta Cryst.* E**68**, o1417.

Werling, K. A., Griffin, M., Hutchison, G. R. & Lambrecht, D. S. (2014). *J. Phys. Chem. A*, **118**, 7404–7410.

Wolff, S. K., Grimwood, D. J., McKinnon, J. J., Turner, M. J., Jayatilaka, D. & Spackman, M. A. (2012). *CrystalExplorer 3.1.* University of Western Australia.

Yadav, H., Sinha, N., Goel, S., Hussain, A. & Kumar, B. (2016). *J. Appl. Cryst.* **49**, 2053–2062.

Yadav, H., Sinha, N. & Kumar, B. (2014). *CrystEngComm*, **16**, 10700–10710.

Yadav, H., Sinha, N. & Kumar, B. (2016). *Cryst. Growth Des.* **16**, 4559–4566.

Zedan, I. T., El-Ghamaz, N. A. & El-Menyawy, E. M. (2015). *Mater. Sci. Semicond. Process.* **39**, 408–415.